ACS Photonics

Letter

Cite This: ACS Photonics XXXX, XXX, XXX−XXX

pubs.acs.org/journal/apchd5

High Spectral Resolution Plasmonic Color Filters with Subwavelength Dimensions

Dagny Fleischman,[†] Katherine T. Fountaine,[‡] Colton R. Bukowsky,[†] Giulia Tagliabue,[†] Luke A. Sweatlock,[‡] and Harry A. Atwater*[,†]

[†]Thomas J. Watson Laboratories of Applied Physics, California Institute of Technology, Pasadena, California 91125, United States

[‡]Northrop Grumman NG Next, One Space Park, Redondo Beach, California 90250, United States

Supporting Information

ABSTRACT: Rapid advances in image sensor technology have generated a mismatch between the small size of image sensor pixels and the achievable filter spectral resolution. This mismatch has prevented the realization of chip-based image sensors with simultaneously high spatial and spectral resolution. We report here a concept that overcomes this trade-off, enabling high spectral resolution (transmission FWHM <31 nm) filters with subwavelength dimensions operating at optical and near-infrared wavelengths. An inverse design methodology was used to realize a new type of plasmonic cavity that efficiently couples an in-plane Fabry−Perot resonator to a single plasmonic slit that supports surface plasmon polaritons. This design principle, combined with a new metal imprinting method that yields metallic nanostructures with both top and bottom surfaces that are extremely smooth, enabled demonstration of high spectral resolution transmission filters with smaller area than any previously reported.

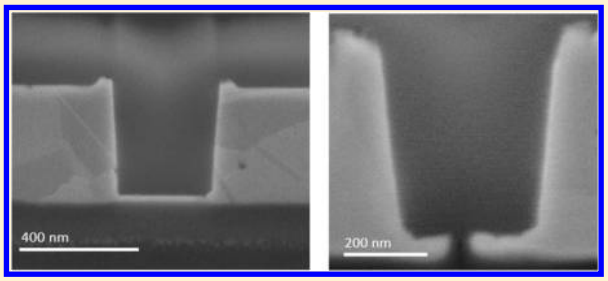

KEYWORDS: *nanophotonics, plasmonics, multimode structures, nanostructures, multispectral filtering, inverse design*

The concept of dimensional scaling has been a cornerstone of solid-state integrated device technology over the past 50 years, fueling "Moore's law" performance advances in silicon integrated circuits,[1] magnetic memories,[2] and optical fiber data transmission,[3] among others. Dimensional scaling of pixel size from over 10 μm to as small as 1.1 μm in CMOS digital image sensor arrays over the past decade has led to greatly increased electronic image resolution, accomplished by coupling an objective lens to a focal plane area populated by an ever-increasing number of pixels at constant array size.[4] These image sensors utilize filters composed of dye-doped polymers that allow them to transmit incident light over red, green, and blue ranges of the visible spectrum to form a color image. Such dye-based color filters typically do not allow for high spectral resolution but are adequate for three-color imaging. Many alternative color filter concepts based on resonances in nanophotonic structures have been explored in an attempt to improve upon the transmission efficiency, spectral resolution, and spatial resolution of dye-based color filters, which suffer from issues with optical cross-talk at small length scales and degradation under UV radiation.[3] Successful demonstrations of hole and slit array filters have relied on short-range order, achieving footprints as small as 1 μm.[4,5] However, these small footprint filters possess relatively large transmission bandwidths, on the order of 100−150 nm, sufficient for three-color imaging but not for multispectral or hyperspectral imaging. However, if filters could be realized that feature transmission bandwidths less than 30 nm, rather than filtering just three colors, imaging systems could be designed to spectrally separate the visible and near-infrared spectrum into 20 colors or more, enabling acquisition and construction of an optical spectrum at every pixel in an image.[6,7] This type of data collection, termed hyperspectral imaging, provides image sensors with the ability to perform spectroscopy at every pixel in an image. The ability to perform multispectral and hyperspectral imaging functions using a compact CMOS image sensor without any moving parts would have far-reaching impacts in fields as disparate as healthcare, food quality control, and space exploration[8−10]

While there have been demonstrations of nanophotonic color filter architectures capable of producing narrow transmission bandwidths, these filters are large, because they rely on medium- to long-range periodic effects to produce their narrow spectral features.[11−14] Guided-mode resonance filters (GMRs) utilize a transmissive waveguide grating to produce a resonant response.[12] The resolving power ($\lambda/\Delta\lambda$) of the transmission band is directly related to the number of periods.[15] To achieve a narrow spectral resonance, GMR filters require approximately 50 lattice periods, which gives them a spatial footprint on the 10's of micrometers at optical wavelengths, making them far too large to serve as color filters in CMOS image sensors.[15]

This relationship between quality factor and lattice periodicity is not particular to GMR filters but is related to the spatial-spectral transform relations of periodically structured media. In general, as the number of periods (N) in a filter increases, so

Received: November 26, 2018
Published: January 2, 2019

DOI: 10.1021/acsphotonics.8b01634
ACS Photonics XXXX, XXX, XXX−XXX

does the spectral resolving power. As shown in Figure 1 for experimental results, hole array filters, single film slit array filters,

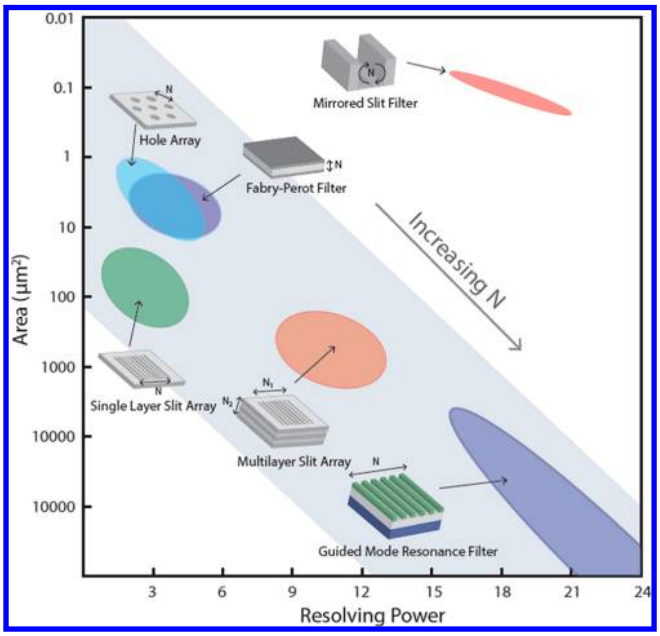

Figure 1. Relationship between the spatial area of a filter and its resolving factor ($\lambda/\Delta\lambda$) for transmission color filters in the visible part of the spectrum. The general trend is shown in the gray region, where smaller footprint filters possess large spectral features and larger footprint filters possess smaller spectral features. This relationship is dictated by N, the number of periods contained within the filter. This relationship is broken by the mirrored slit filter (small red oval), because the mirrors create an effectively large number of periods within a very confined space.

and single film Fabry–Perot resonant filters can all exhibit relatively small footprints, but their experimental spectral transmittances are broad, and color separation is limited to three or four spectral bands.[4,5,16,17] Multilayer slot mode plasmonic color filters introduced an additional dimension of periodicity, which allowed for a narrower response, but the footprint of these filters, while smaller than GMR filters, is still too large for the smallest pixel image sensor applications.[11]

While this relationship is shown for the spatial area in Figure 1, this trend also holds for the volume of color filters. In general, the larger the volume of the filter, the narrower the transmission response, as shown by the narrowing of the spectral response of Bragg gratings as their number of periods increases.[18]

Reflective boundaries at the edges of a smaller footprint all-dielectric microwave GMR filter have been used to create a synthetic long-range order in smaller footprint structures.[19] In this paper, we use highly reflective metal boundaries on a single plasmonic slit to break the relationship illustrated in Figure 1 between footprint and periodicity. The metal mirrors in the mirrored filter impose effective periodic boundary conditions on the transmission slit, which in the lossless limit would introduce infinite periodicity into a small-footprint structure. These filters are simultaneously smaller than any color filter described in the literature and possess a resolving power on par with the highest performing nanophotonic visible light color filters that benefit from long-range order effects.

The mirrored filters possess highly coupled parameters that can be used to control the filters' performance. The schematic shown in Figure 2(a) shows the main parameters considered during the optimization of these filters: mirror height, mirror spacing, slit width, film thickness, and oxide thickness. The general design of the mirrored color filter takes advantage of multiple resonances within the structure. A gap mode, shown in Figure 2(b), is supported in the deeply subwavelength slit that penetrates the thin film. Figure 2(c) shows a cavity mode supported by two vertical mirrors, where the available cavity modes are dictated by the mirror spacing, mirror height, and oxide thickness. These modes can be used to produce narrowband spectral responses in Fabry–Perot filters.[14] The thin film also supports surface plasmon polariton modes (SPPs) on its top and bottom surfaces. A top surface SPP mode is shown in Figure 2(d). SPP modes have been used to produce transmission color filtering when incorporated into a grating structure. In addition to these three types of modes, there are numerous other modes supported by this structure. However, the transmission filters that exhibit high spectral resolution are characterized by coupling of these three modal types to achieve narrowband filter performance. By optimizing a structure to be resonant at specific wavelengths, it is possible to produce narrow-bandwidth transmission color filtering.

As demonstrated by Supplemental Figures 1 and 2, two of the features most responsible for the narrowband transmission response are the efficiency of the gap mode and the thickness of the thin film spanning the distance between the two reflective mirrors. The coupling efficiency of the gap mode dictates the overall transmission intensity of the filter. Without the ability to efficiently couple into the gap mode excitation, the overall transmission response is low. The line width of the transmission response was shown to strongly depend on the thickness of the metal film. When the metal film is thin, excited modes can couple across it, which leads to a much narrower transmission response, even when all other physical parameters are held fixed. While these two aspects of the filter play a large role in the transmission response, changes to any of the filter dimensions were found to affect the coupling of the excited modes and the resulting transmission of the filters. The height and spacing of the mirrors, the thickness of the thin film, the slit width, the high index oxide coating thickness, and the materials chosen as the metal and dielectric components all affect the filter transmission efficiency and line width.

Even for a fixed set of chosen dielectric and metallic materials, the number of parameters is too high and their relationships too complex to effectively optimize filter transmission efficiency and line width by heuristic analysis and inductive physical reasoning alone. To ensure a strong candidate filter was identified, a numerical optimization method was used to design the champion filter fabricated in this study. The Nonlinear Mesh Adaptive Direct Search algorithm (NOMAD) was selected to optimize this structure because of its computational efficiency and the ability to use surrogate functions.[20−22] After the surrogate function is approximated, this hybrid global and local search method alternates between searching and polling on a mesh of points within the parameter space. The resolution of this mesh is adjusted by the algorithm to allow for addressing both coarse and fine probing within the parameter space, which facilitates both efficiently finding the optimum value and preventing the algorithm from getting trapped in local minima. The figure of merit (FOM) used for spectrally narrowband transmission filter design accounts for the spectral constraints on the filter,

DOI: 10.1021/acsphotonics.8b01634
ACS Photonics XXXX, XXX, XXX−XXX

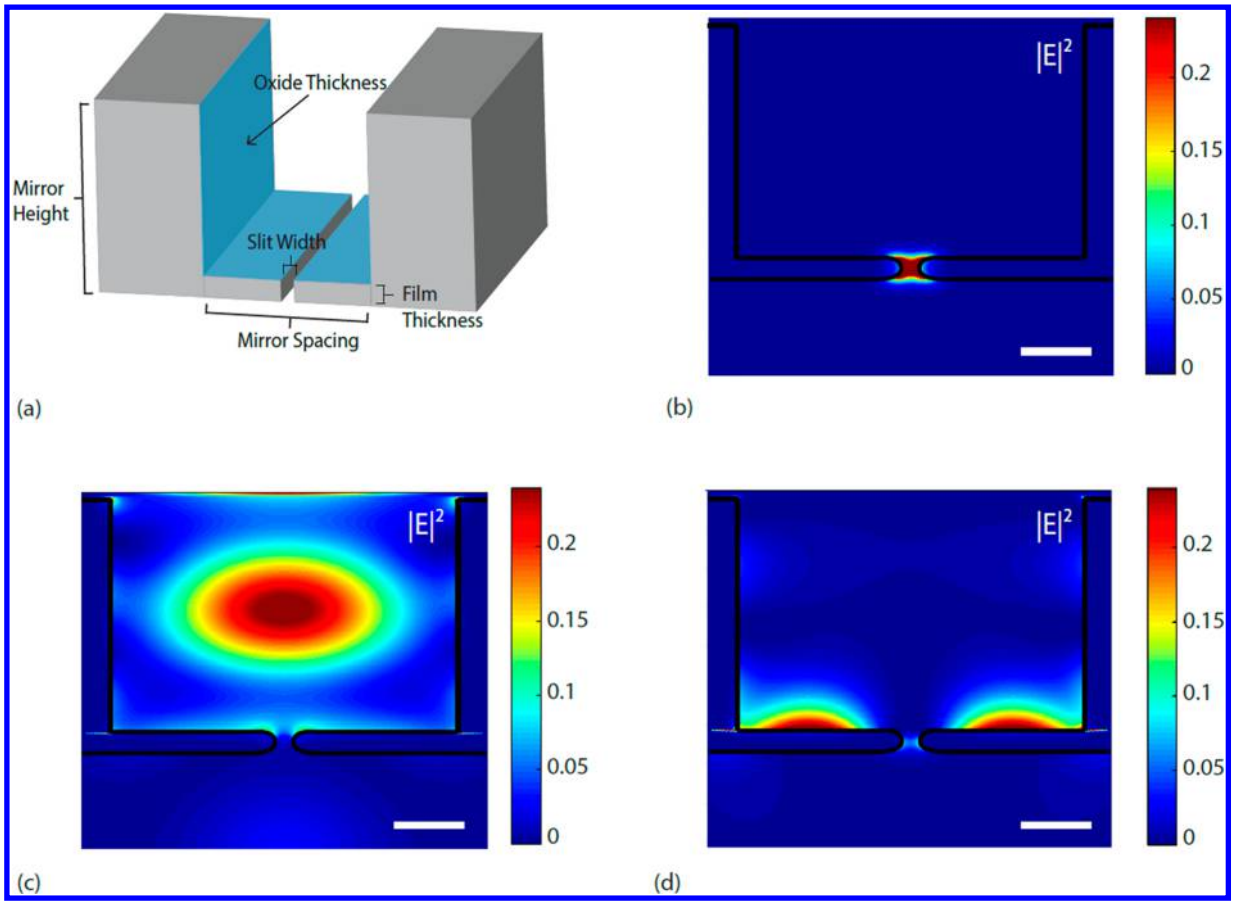

Figure 2. (a) Schematic of the narrowband transmission filter showing the main structure parameters: film thickness, mirror height, mirror spacing, slit width, and oxide thickness (shown in blue). The optimal filter was found to possess a film thickness of 48 nm, mirror height of 598 nm, slit width of 31 nm, and oxide thickness of 1 nm for a variety of mirror spacings. (b) Electric field intensity profile for sample eigenmode solutions for a mirrored slit filter illustrating the gap mode within the slit in the thin film with behavior controlled by the slit width and film thickness. (c) Electric field intensity profile for the cavity mode contained between the two mirrors with behavior controlled by the mirror height, mirror spacing, and oxide thickness. (d) Electric field intensity profile for surface plasmon polariton mode supported on the surface of the thin film with behavior controlled by the film thickness, oxide thickness, mirror spacing, and slit width. The scale bar in (b)−(d) is 100 nm.

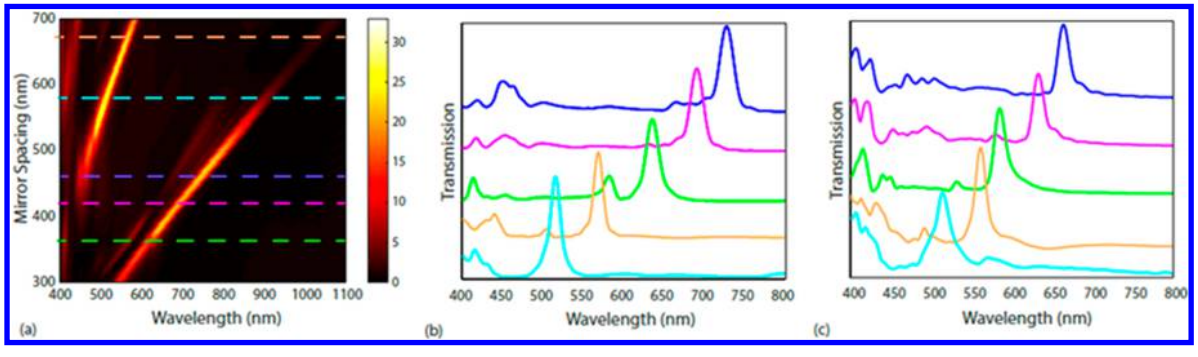

Figure 3. (a) Superposition of transmission plots illustrating the effect of mirror spacing on transmission peak position for 2D linear filters. There are two active mode orders in the visible spectrum: the longer wavelength transmission band corresponds to the lowest order cavity mode and the shorter wavelength band corresponds to the first higher order cavity mode. (b) Simulated transmission response of the optimized 2D linear filter for a few mirrored filters spanning the visible part of the spectrum. (c) Simulated transmission response of a few 3D square filters with the same mirror spacings as the filters shown in (b).

$$\mathrm{FOM} = (\Delta wav/c.wav) + (c.peak/peak) + (noise/c.noise) + (FWHM/c.FWHM)$$

This relation seeks to maximize the intensity of a single peak at the desired wavelength (*peak*) while minimizing both the FWHM (*FWHM*) of that peak and the intensity of any additional peaks (*noise*). It also seeks to shift the maximum intensity of the peak to the intended transmission band of the filter (Δwav). Each term has a weighting factor (*c.wav*, *c.peak*, *c.noise*, and *c.FWHM*) that can be used to enhance or suppress the effect of a given term in the FOM. These weighting factors were varied during the study, but the champion filter identified had the following weighting factors: *c.wav* = 0.1, *c.peak* = 1, *c.noise* = 5, *c.FWHM* = 5 to yield a filter with Δwav = 0.5 nm, peak

DOI: 10.1021/acsphotonics.8b01634
ACS Photonics XXXX, XXX, XXX−XXX

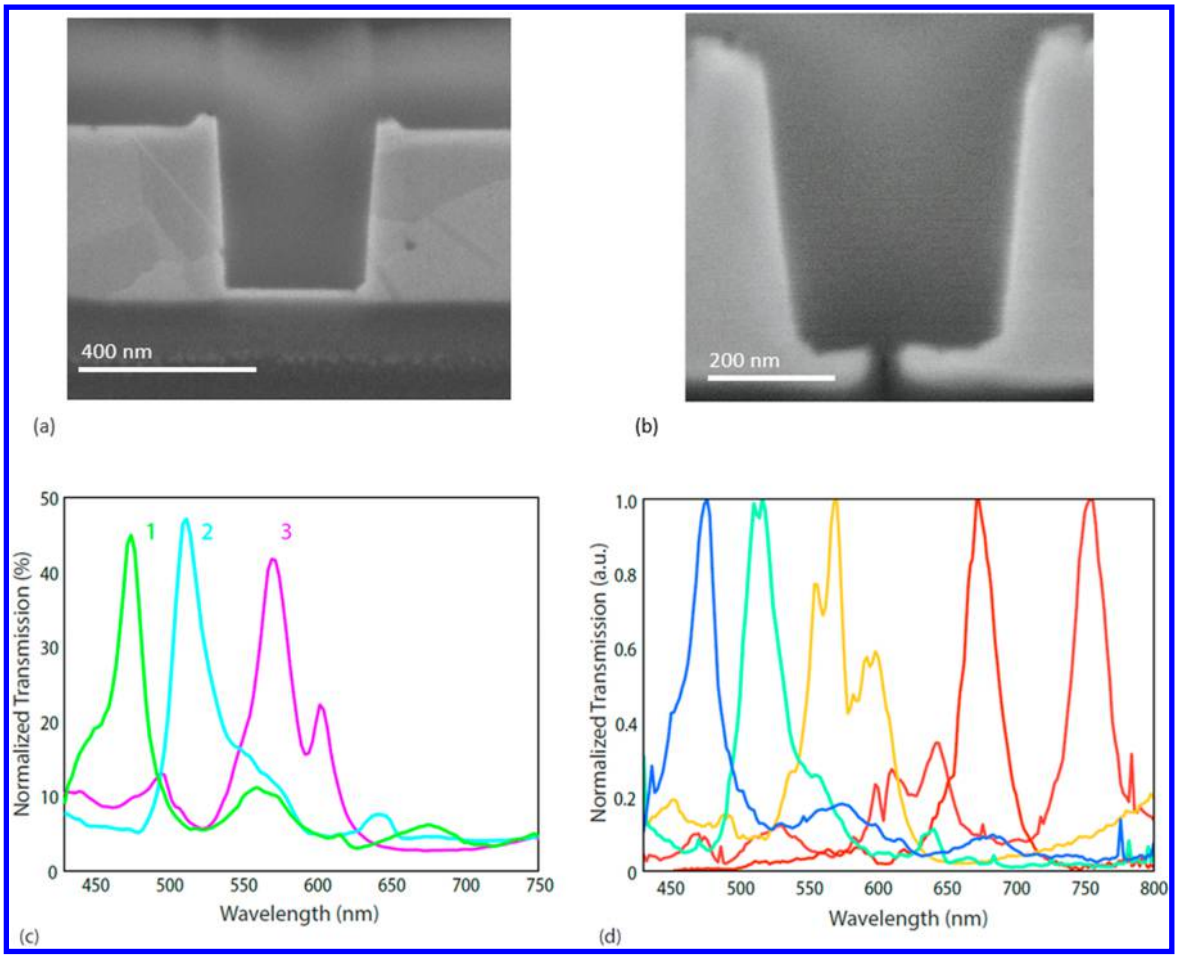

Figure 4. (a) Cross-section of a thinned filter prior to the aligned mill of the slit. (b) Cross-section of a completed filter. The images are both tilted to 52°, exaggerating the apparent taper. The measured tapers of the mirrors of these filters are both less than 3°. (c) Measured transmission spectra for three linear color filters. Each possesses a FWHM of 31 nm or less and a cross-sectional footprint of less than 600 nm. (d) Transmission measurements of five linear color filters plotted in the CIE color of their transmission peak. Each filter was normalized to its peak transmission value to emphasize its narrow transmission bandwidth and high signal-to-noise ratio.

= 25.3%, noise = 49, and FWHM = 15 nm. The optimization produced a spread of FOMs, starting as high as 330 and reaching as low as 16.7. To develop the champion filter shown in Figure 2(a), five parameters were varied: mirror height, mirror spacing, slit width, film thickness, and the thickness of a HfO_2 layer coating the metal filter. We also found that while additional slits can be used to improve the overall transmission intensity of the color filter, these additional slits increase the footprint of the filter, so the number of slits was fixed to one. The spacing between the mirrors of this optimized filter is 618 nm. The fields of the modes supported by the structure were calculated to penetrate 46 nm into each mirror, leading to a full footprint of 710 nm.

The transmission peak of the optimized filter can be shifted across the spectrum by changing the position of the mirrors. Figure 3(a) shows a superposition of transmission curves for filters with different mirror spacing for linear filters in a 2D simulation environment. The superposition plot indicates there are two active transmission bands in the visible part of the spectrum, one corresponding to shorter wavelengths and one corresponding to longer wavelengths. The FWHM of these optimized filters varied from 14 to 26 nm across the visible spectrum. The FWHM of these filters is in large part dictated by the optical loss present in Ag. We also investigated filter design for the same structures under the assumption of a metal that acts as a perfect electric conductor. In these lossless structures, filter structures were found to exhibit FWHM values as low as 7 nm.

We explored the mode orders associated with these transmission bands using an eigenmode solver, and the results indicated that the longer wavelength band is due to the lowest order cavity mode, while the shorter wavelength transmission arises from the second-order cavity mode. To further illustrate the transmission response, Figure 3(b) shows a few representative transmission spectra for linear filters with a single slit. Between the two different transmission bands these filters possess narrowband transmission behavior across most of the visible and part of the near-IR portions of the spectrum. To demonstrate that the principles at work in the performance of the two-dimensional filters also apply for three-dimensional filters composed of two crossed slits instead of a linear slit, three-dimensional simulations were performed for the same geometrical parameters and materials used in the two-dimensional filters. The results of these simulations are shown in Figure 3(c) and illustrate that despite the sub-micrometer areas of three-dimensional filters, the resonant modes excited in the three-dimensional structures are similar to those seen in two-dimensional filters.

DOI: 10.1021/acsphotonics.8b01634
ACS Photonics XXXX, XXX, XXX−XXX

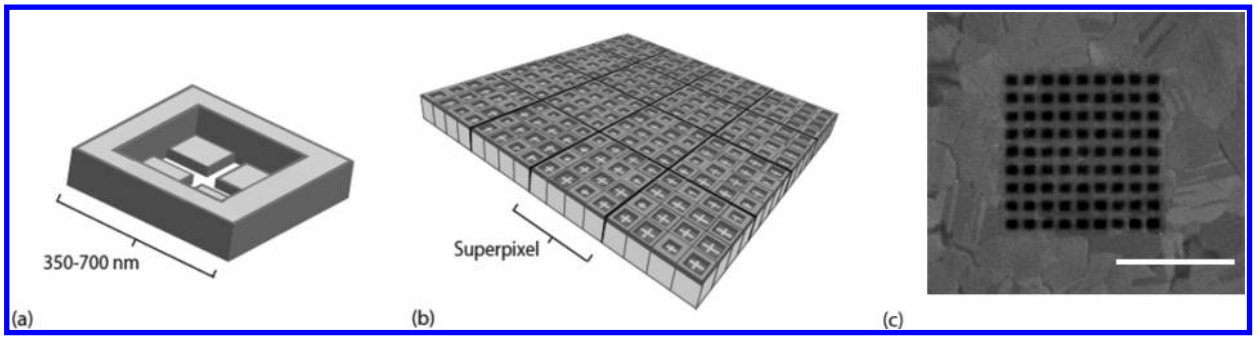

Figure 5. (a) Schematic of a single square filter. The footprint of each side varies from 350 to 700 nm for filters in the visible part of the spectrum. (b) Schematic of a proposed multispectral "superpixel" composed of arrays of ultracompact square filters. (c) Electron micrograph of a 9 × 9 array of 424 nm to a side square filters. The dark contrast squares are the SiO_2 pillars between the lighter contrast mirrors. All filters in this array are spaced 200 nm apart and the scale bar is 5 μm.

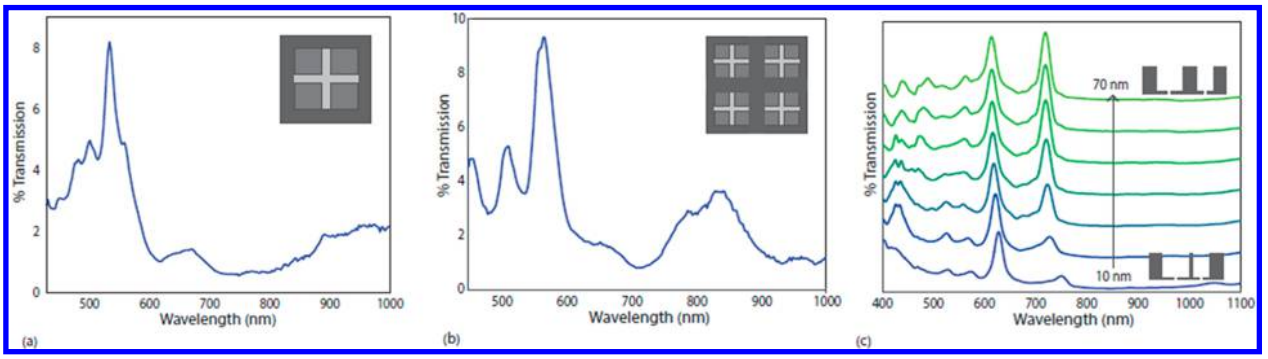

Figure 6. (a) Transmission spectrum for a single square filter that has an edge-length of 692 nm. (b) Transmission spectrum for a 2 × 2 array of square filters. Each filter has edge-lengths of 424 nm, and they are spaced 200 nm apart. The single narrow peak experimentally verifies that square filters produce the expected response and arrays of pixels do not possess optical crosstalk. (c) Calculated crosstalk between two spectrally distinct linear filters. The width of the mirror separating the two active filter areas varies from 10 nm (blue) to 70 nm (green). There is no evidence of optical crosstalk in filters spaced at least 50 nm apart.

The sidewalls of the mirrors were found to strongly affect filter transmittance. Slight changes to the mirror spacing or sidewall taper can dramatically change filter performance. To closely control the quality of the mirrors, the filters were fabricated using a novel metal imprinting method. This method, described in the Supporting Information, produces metallic nanostructures with extremely smooth metal surfaces on both sides, as illustrated in Figure 4(a) and (b). While template stripping methods are able to produce a very smooth surface on one side of the metallic structure,[23] the other surface has a roughness defined by metallic grain growth during vapor deposition. By contrast, our metal imprinting method yields equivalently smooth surfaces on both sides, which is critical to narrowband filter performance. The imprinting method was also found to yield straighter, smoother, and more vertically oriented metallic sidewalls than is achievable via either metal etching or lift-off processing.

The fabricated filters were measured using a supercontinuum laser incident upon a monochromator that is focused through a home-built focusing setup and a 50× objective to yield a Gaussian beam with a 2 μm spot size. A beam sampler directed some of the incident power to a reference diode that was used to ensure the consistent normalization of all spectra. Multiple filter geometries were measured to verify the spectral response of the simulated filters. Due to the subdiffraction limit footprint of all filters, they were all normalized relative to the 5 μm aperture. This relatively large aperture was chosen to prevent any resonant effects in the normalization spectrum. If a smaller aperture were used, it would add resonant features into the transmission response that would be convolved with the transmission spectrum of the filter. While the 2 μm beam spot still allowed for the filters to report relatively high transmission efficiencies, these values would be even higher if considered relative to the 1 μm footprint of state-of-the-art CMOS pixels. Normalization was also used to account for the spurious scattered background signal reported by the measurement setup in the near-IR.

Three transmission spectra for different linear color filters are shown in Figure 4(c). The linear filters are polarization dependent, and each has a footprint of less than 600 nm in the lateral direction. Filter 1 demonstrated peak transmission at 475.0 nm, indicating that while these filters are made with Ag, they can still perform at wavelengths less than 500 nm. The FWHM of this filter is 24.8 nm, corresponding to a resolving power of 19.2. Filter 2 shows similar behavior at peak position 512.5 nm, FWHM 30.6 nm, and resolving power 16.7. Filter 3's peak at 570.0 had a FWHM and resolving power of 31.5 nm and 18.1, respectively. There is a small side-lobe on filter 3, which we suggest is due to a slight misalignment of the filtering slit. Each filter was normalized to a 5 μm square hole through the Ag and reported a normalized transmission of at least 40%, despite the sub-micrometer width of each slit filter. The footprint of filter 3 is 0.65 that of filter 2, which was used as an additional normalization factor to account for the reduced amount of light incident on that filter. The measured filters also demonstrated high signal-to-noise ratios, indicating that they are well-suited for application in hyperspectral filtering. Figure 4(d) illustrates the normalized transmission spectra for filters with transmission bands varying across the visible range. These filters were

DOI: 10.1021/acsphotonics.8b01634
ACS Photonics XXXX, XXX, XXX−XXX

measured using a transmission confocal setup with a 5 μm circular pinhole aperture (shown in Supplemental Figure 6(c)), which mimics the detection configuration of color filters integrated into CMOS image sensors. In general, the measured filters show excellent agreement with simulation, and the experimental filters possess enhanced transmission that we suggest is due to the very large grain and smooth surfaces of the Ag, which reduces loss within the system.[24] The experimental filter results validate that the mirrored filter design is capable of breaking the relationship between footprint and resolving power within nanophotonic filters. These filters can produce narrowband transmission spectra with just a single period of the nanophotonic feature.

In a multispectral or hyperspectral image sensor, individual filters are architected in pixel arrays. A potential layout geometry is shown in Figure 5 in which individual square filters (Figure 5(a)) are arrayed into superpixels (Figure 5(b)) that each correspond to a single spatial coordinate, and the filters are all separated by the width of the mirrors that surround the active filtering area. A fabricated array of filters is shown in Figure 5(c). The dark gray squares are the SiO_2 regions between the lighter gray 200 nm wide mirrors. Experimental results for the three-dimensional square filters are shown in Figure 6(a) and (b). In Figure 6(a) the transmission results for a single square filter with mirror-to-mirror spacing of 692 nm is shown normalized to a 5 μm aperture. The transmission response demonstrates that a sharp feature can be produced, even for a sub-micrometer single filter. The noise around the peak is due to fabrication imperfections in individual filters and as can be seen by comparison with spectrally averaged measurements from multiple square filters, as shown in Figure 6(b), where a 2 × 2 array of the same square filters was measured. Each filter has an edge length of 424 nm, and the spacing between the filters is 200 nm. The filters are each spaced less than 200 nm apart, and there is no evidence of optical crosstalk between the filters. The leftmost secondary peak is evident in simulations of single pixels of this structure. Slight misalignments of the milled crosses within each filter area are responsible for the slight broadening of this peak, which is less evident in the single filter case. We suggest the other two smaller peaks are also due to these fabrication imperfections. Calculations further demonstrate that not only can the same wavelength filters be arrayed close together, so can filters targeting different wavelengths. Figure 6(c) illustrates an array of simulations where the spacing between two adjacent filters was varied from 10 to 70 nm. The two peaks at 612.2 and 718.1 nm correspond to the transmission bands of the individual filters. Once the spacing between the filters exceeds the skin depth of Ag, 50 nm at these wavelengths, there is no evidence of optical crosstalk between the filters. This indicates that in a device filters can be spaced as close as 50 nm apart without introducing artifacts from optical crosstalk.

By coupling an in-plane Fabry−Perot resonator to a surface plasmon polariton mode, and utilizing a novel metal imprint fabrication method for filter fabrication, we were able to design ultracompact narrowband transmission color filters that break the relationship between footprint and resolving power. Filters were experimentally shown to achieve narrowband spectral filtering and function in pixel arrays. The filtering mechanism is not dependent on any absolute length scale, so larger filters can be used to filter longer wavelength light utilizing Ag or other material systems. For example, filters employing Cu mirrors are extremely effective at filtering light in the near-IR part of the spectrum, as shown in Supplemental Figure S7. Additionally, while these filters are static, introducing a gate-tunable dielectric such as indium tin oxide could potentially be used to spectrally tune the peak transmission wavelength and thus reduce the number of filters needed to form a superpixel without reducing the spectral resolution.

METHODS

Optimization Method. The process for optimizing the filter structure using the NOMAD algorithm and the FOM (equation above) is illustrated in Supplemental Figure 3. All steps are performed automatically after the optimization process is initiated, using the optimization defaults unless indicated in Supplementary Table 2. In this method, the algorithm suggests a set of physical parameters for the filter. The Lumerical finite difference time domain simulation package (FDTD), an eigenmode solver, then use these parameters to perform a simulation to determine the filter's optical response. The resulting transmission spectrum of the filter is then analyzed by a custom peak-finding algorithm, which was developed to include both the maxima at the edges of a vector and plateaus, to make sure that all peak-like features would be properly identified and accounted for. Using the analyzed spectrum, the FOM is calculated and used by NOMAD to suggest a new set of physical parameters. This process repeats until the convergence criteria are met.

Fabrication Method. The sidewalls of the mirrors closely control the transmission behavior of the filters. Slight changes to the mirror spacing or taper can dramatically change the filter performance. To closely control the quality of the mirrors, the filters were fabricated using a metal-imprinting process. This method, shown in Supplemental Figure 4, produces mirrors with straighter sidewalls than lift-off processing with the added benefit of producing extremely smooth metal structures.

The fabrication method is discussed in detail in the Supporting Information, and a schematic of the process flow is provided in Supplemental Figure 4. The method consists of four main steps: defining the SiO_2 structures that form the negative space around the metal mirrors using electron beam lithography and dry etching, infilling the Ag mirrors with electron beam deposition and a metal imprinting process, removing excess Ag and smoothing the remaining metal with a dry etch and the imprinting method, then milling the slit in the metal film and encapsulating with insulating materials.

Measurement Setup and Analysis. Transmission measurements were performed with a custom-built optical setup that uses an NKT SuperK Extreme white laser as the light source. As shown in Supplemental Figure 6, the beam was monochromated with variable slit width to give a constant bandpass of 2 nm, collimated, expanded by two 90° off-axis parabolic mirrors, and finally focused onto the sample with a long working distance, low-NA objective (Mitutoyo Plan Apo 50×, tube length 200 mm, NA = 0.55). A CMOS (IDS UI-1460SE) camera was used to experimentally characterize the beam shape at the focal plane and verify it had a FWHM of ∼2 nm. The setup was used in this configuration to perform the measurements of the linear filters shown in Figure 4(c) and the crossed filters shown in Figure 6.

To confirm there were no artifacts from background signal present in these measurements, the background signal needed to be further attenuated so the above setup was modified into a transmission confocal microscopy configuration. The same monochromatic and collimated beam was redirected 180° via mirrors to enter the objective passing through its focal point. A second objective, pinhole, and low dark current photodiode

DOI: 10.1021/acsphotonics.8b01634
ACS Photonics XXXX, XXX, XXX−XXX

were incorporated into the beam path to perform these measurements. Peak-normalized signal-to-noise (SNR) plots were created using this method because it significantly increased spatial signal contrast and greatly reduced the background spectrum such that subpercent peaks could be detected without a loss in SNR. The normalization spectrum for each filter was measured on an area of the fused silica superstrate where no Ag film existed, which accounted for the reflection of the superstrate. The specific method for calibration and the details for the remaining components in the optical beam path are described in detail in the Supporting Information.

■ ASSOCIATED CONTENT

Supporting Information

The Supporting Information is available free of charge on the ACS Publications website at DOI: 10.1021/acsphotonics.8b01634.

Additional information about the nature of the behavior of the transmission color filters, the optimization method, the fabrication method, and the measurement setup and analysis (PDF)

■ AUTHOR INFORMATION

Corresponding Author

*E-mail: haa@caltech.edu.

ORCID

Harry A. Atwater: 0000-0001-9435-0201

Author Contributions

D.F. and H.A.A. conceived of the ideas. K.F. formatted the optimization code, built the peak finding algorithm, and designed the FOM with input from D.F. D.F. used the optimization code to identify the filter geometry. D.F. developed the fabrication method and made the filters. G.T. and C.B. built the measurement setup. D.F. and C.B. took the measurements, and G.T. contributed to data analysis. D.F. and H.A.A. cowrote the paper. All authors discussed the results and commented on the manuscript, and H.A.A. supervised.

Notes

The authors declare no competing financial interest.

The data that support the findings of this study are available from the corresponding author upon reasonable request.

■ ACKNOWLEDGMENTS

This work was supported by the Air Force Office of Scientific Research under grant number FA9550-16-1-0019. G.T. acknowledges support from the Swiss National Science Foundation through the Advanced Mobility Fellowship, Grant P300P2_171417. D.F. gratefully acknowledges Artur Davoyan, Matt Sullivan Hunt, Michelle Sherrott, Phil Jahelka, and Sisir Yalamanchili for useful discussions during the development of this work.

■ REFERENCES

(1) Moore, G. E. Cramming More Components onto Integrated Circuits. *Proc. IEEE* **1965**, *86*, 82−85.

(2) Thompson, D. A.; Best, J. S. The Future of Magnetic Data Storage Techology. *IBM J. Res. Dev.* **2000**, *44*, 311−322.

(3) Hecht, J. Is Keck's Law Coming to an End. *IEEE Spectr* **2016**, 11−23.

(4) Horie, Y.; Han, S.; Lee, J.-Y.; Kim, J.; Kim, Y.; Arbabi, A.; Shin, C.; Shi, L.; Arbabi, E.; Kamali, S. M.; et al. Visible Wavelength Color Filters Using Dielectric Subwavelength Gratings for Backside-Illuminated CMOS Image Sensor Technologies. *Nano Lett.* **2017**, *17*, 3159−3164.

(5) Yokogawa, S.; Burgos, S. P.; Atwater, H. A. Plasmonic Color Filters for CMOS Image Sensor Applications. *Nano Lett.* **2012**, *12*, 4349−4354.

(6) Chen, Q.; Hu, X.; Wen, L.; Yu, Y.; Cumming, D. R. S. Nanophotonic Image Sensors. *Small* **2016**, *12*, 4922−4935.

(7) Jang, W.-Y.; Ku, Z.; Jeon, J.; Kim, J. O.; Lee, S. J.; Park, J.; Noyola, M. J.; Urbas, A. Experimental Demonstration of Adaptive Infrared Multispectral Imaging Using Plasmonic Filter Array. *Sci. Rep.* **2016**, *6*, 34876.

(8) Yudovsky, D.; Nouvong, A.; Pilon, L. *Hyperspectral Imaging in Diabetic Foot Wound Care*; SAGE Publications Sage CA: Los Angeles, CA, 2010.

(9) Gowen, A. A.; O'Donnell, C. P.; Cullen, P. J.; Downey, G.; Frias, J. M. Hyperspectral Imaging − an Emerging Process Analytical Tool for Food Quality and Safety Control. *Trends Food Sci. Technol.* **2007**, *18*, 590−598.

(10) Hege, E. K.; O'Connell, D.; Johnson, W.; Basty, S.; Dereniak, E. L. Hyperspectral Imaging for Astronomy and Space Surveillance. *Proc. SPIE* **2003**, *5159*, 380−391.

(11) Fleischman, D.; Sweatlock, L. A.; Murakami, H.; Atwater, H. Hyper-Selective Plasmonic Color Filters. *Opt. Express* **2017**, *25*, 27386−27395.

(12) Wang, S. S.; Magnusson, R. Theory and Applications of Guided-Mode Resonance Filters. *Appl. Opt.* **1993**, *32* (14), 2606−2613.

(13) Mazulquim, D. B.; Lee, K. J.; Yoon, J. W.; Muniz, L. V.; Borges, B.-H. V.; Neto, L. G.; Magnusson, R. Efficient Band-Pass Color Filters Enabled by Resonant Modes and Plasmons near the Rayleigh Anomaly. *Opt. Express* **2014**, *22*, 30843−30851.

(14) Macleod, H. A.; Macleod, H. A. *Thin-Film Optical Filters*; CRC Press, 2010.

(15) Grepstad, J. O.; Greve, M. M.; Holst, B.; Johansen, I.-R.; Solgaard, O.; Sudbø, A. Finite-Size Limitations on Quality Factor of Guided Resonance Modes in 2d Photonic Crystals. *Opt. Express* **2013**, *21*, 23640−23654.

(16) Yoon, Y.-T.; Lee, S.-S. Transmission Type Color Filter Incorporating a Silver Film Based Etalon. *Opt. Express* **2010**, *18*, 5344−5349.

(17) Zeng, B.; Gao, Y.; Bartoli, F. J. Ultrathin Nanostructured Metals for Highly Transmissive Plasmonic Subtractive Color Filters. *Sci. Rep.* **2013**, *3*, 2840.

(18) Čtyroký, J.; Gonzalo Wangüemert-Pérez, J.; Kwiecien, P.; Richter, I.; Litvik, J.; Schmid, J. H.; Molina-Fernández, Í.; Ortega-Moñux, A.; Dado, M.; Cheben, P. Design of Narrowband Bragg Spectral Filters in Subwavelength Grating Metamaterial Waveguides. *Opt. Express* **2018**, *26*, 179.

(19) Barton, J. H.; Rumpf, R. C.; Smith, R. W.; Kozikowski, C. L.; Zellner, P. A. All-Dielectric Frequency Selective Surfaces with Few Number of Periods. *Prog. Electromagn. Res.* **2012**, *41*, 269−283.

(20) Rios, L. M.; Sahinidis, N. V. Derivative-Free Optimization: A Review of Algorithms and Comparison of Software Implementations. *J. Glob. Optim.* **2013**, *56*, 1247−1293.

(21) Audet, C.; Dennis, J. E. J. Mesh Adaptive Direct Search Algorithms for Constrained Optimization. *SIAM J. Optim.* **2006**, *17*, 188−217.

(22) Le Digabel, S. Algorithm 909: NOMAD: Nonlinear Optimization with the MADS Algorithm. *ACM Trans. Math. Softw.* **2011**, *37*, 44:1−44:15.

(23) Park, J. H.; Nagpal, P.; McPeak, K. M.; Lindquist, N. C.; Oh, S.-H.; Norris, D. J. Fabrication of Smooth Patterned Structures of Refractory Metals, Semiconductors, and Oxides via Template Stripping. *ACS Appl. Mater. Interfaces* **2013**, *5*, 9701−9708.

(24) McPeak, K. M.; Jayanti, S. V.; Kress, S. J. P.; Meyer, S.; Iotti, S.; Rossinelli, A.; Norris, D. J. Plasmonic Films Can Easily Be Better: Rules and Recipes. *ACS Photonics* **2015**, *2*, 326−333.

DOI: 10.1021/acsphotonics.8b01634
ACS Photonics XXXX, XXX, XXX−XXX